

# 6

## Mean field modelling of differential rotation

Gunther Rüdiger

*Astrophysikalisches Institut Potsdam, D-14482, Germany*

Leonid L. Kitchatinov

*Institute for Solar-Terrestrial Physics, P.O. Box 4026, Irkutsk 664033, Russia  
and Astrophysikalisches Institut Potsdam, D-14482 Potsdam, Germany*

### Abstract

Analytical expressions for the  $\Lambda$ -effect and the heat conductivity tensor for rotating turbulent convection are compared with current results of box simulations with the NIRVANA code. With these results the large-scale flow pattern (rotation plus meridional circulation) in the convection zone is computed in good agreement with the observations. The penetration of the meridional flow into the subadiabatic layer beneath the convection zone (with viscosity  $\nu_{\text{core}}$ ) appears to vary with  $\sqrt{\nu_{\text{core}}}$  so that in a non-turbulent tachocline the penetration would be extremely small. New mean field model calculations are also presented for the rotation laws in F stars and M dwarfs and finally the question is discussed whether mean-field models may also lead to ‘antisolar’ rotation, i.e. to rotation laws with a decelerated equator.

### 6.1 Introduction

In order to explain the internal rotation of solar/stellar convection zones, the theory of the  $\Lambda$ -effect has been developed. It describes the angular momentum transport in rigidly rotating anisotropic fields of free turbulence. The preferred direction is radial, owing to the stratification of both the density and the intensity of the turbulence.

The cross-correlations  $\langle u'_r u'_\phi \rangle$  and  $\langle u'_\theta u'_\phi \rangle$  of the one-point-correlation tensor  $Q_{ij} = \langle u'_i(\mathbf{x}, t) u'_j(\mathbf{x}, t) \rangle$  provide the radial and latitudinal turbulent transport of angular momentum. For those terms the general formulation

$$Q_{ij} = \dots + A_{ijk} \Omega_k \quad (6.1)$$

has been introduced, or, in more detail,

$$Q_{r\phi} = \nu_T V \Omega \sin \theta, \quad Q_{\theta\phi} = \nu_T H \Omega \cos \theta, \quad (6.2)$$

with  $\nu_T$  as the eddy viscosity. The dimensionless functions  $V$  and  $H$  are normalized expressions for the vertical and horizontal cross-correlations. A quasilinear theory for a special turbulence model has been given by Kitchatinov & Rüdiger (1993, hereafter denoted by KR93) to reveal the dependence on the basic angular velocity  $\Omega$  and the colatitude  $\theta$ . The main result of such analytical calculations for the case of *rapid rotation* can be summarised in the form

$$Q_{r\phi} \simeq -\hat{H} \cos^2 \theta \sin \theta, \quad Q_{\theta\phi} \simeq \hat{H} \sin^2 \theta \cos \theta, \quad (6.3)$$

with positive  $\hat{H}$ . The vanishing of  $Q_{\theta\phi}$  at the equator is a simple consequence of the prevailing symmetries, but the vanishing of  $Q_{r\phi}$  at the equator of a rapid rotator is a surprising and non-trivial result. Also, the signs of the cross-correlations are non-trivial results of the calculations. The resulting angular momentum transport is always inwards ( $V < 0$ ) and equatorwards ( $H > 0$ ). By a direct inspection of the results of helioseismology one finds an increase of angular velocity with depth in the uppermost layers of the solar convection zone, which means that the angular momentum is transported inwards,  $V < 0$  (§6.4). Also, almost all of the presented numerical simulations lead to  $V < 0$  for both slow and fast rotation (see below).

## 6.2 The $\Lambda$ -effect

Quasilinear analytical derivations of the angular momentum transport by rotating turbulence in stratified fluids result in the expressions

$$\begin{aligned} V &= V^{(0)}(\Omega^*) - H^{(1)}(\Omega^*) \cos^2 \theta, \\ H &= H^{(1)}(\Omega^*) \sin^2 \theta, \end{aligned} \quad (6.4)$$

for the normalized fluxes. The coefficients  $V^{(0)}$  and  $H^{(1)}$  depend on the Coriolis number  $\Omega^* = 2\tau_{\text{corr}}\Omega$  (see Figure 6.1 derived from an actual model of the solar convection zone). The usual concept to determine the correlation tensor of density-stratified rotating turbulence is to *prescribe* the turbulence field without rotation and then to derive the influence of rotation on the original turbulence. As the first step in this procedure an anelastic flow ( $\nabla \cdot (\rho \mathbf{u}^{(0)}) = 0$ ) in a non-rotating fluid must be considered. The spectral tensor of the momentum density for such a non-uniform original turbulence is

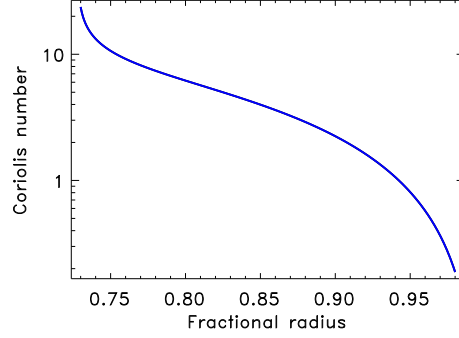


Fig. 6.1. Radial profile of the Coriolis number  $\Omega^*$  for our solar model. The turbulence must be considered as fast (slowly) rotating at the bottom (top) of the convection zone.

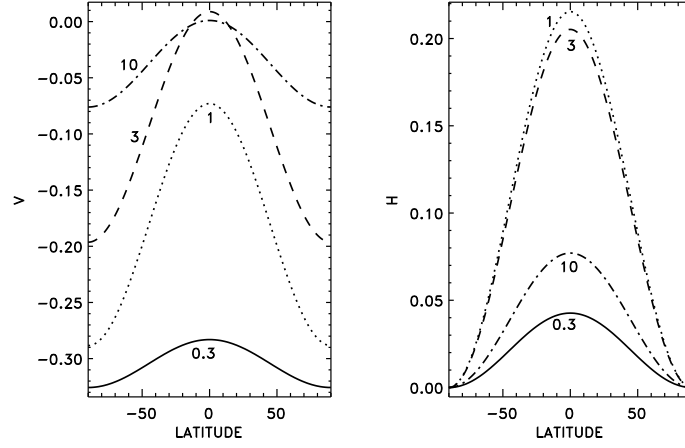


Fig. 6.2. Normalized fluxes of angular momentum as functions of latitude for  $a = 2$ . The lines are marked by the values of  $\Omega^*$ . Note also the clear  $\Lambda$ -quenching by rapid rotation.

$$\begin{aligned}
 \hat{M}_{ij} = & \frac{\hat{E}(k, \omega, \boldsymbol{\kappa})}{16\pi k^2} \left( \delta_{ij} - \left( 1 + \frac{\kappa^2}{4k^2} \right) \frac{k_i k_j}{k^2} + \frac{1}{2k^2} \left( \kappa_i k_j - \kappa_j k_i \right) + \right. \\
 & \left. + \frac{\kappa_i \kappa_j}{4k^2} \right) + \frac{\hat{E}_1(k, \omega, \boldsymbol{\kappa})}{16\pi k^4} \left( \frac{(\mathbf{k} \cdot \boldsymbol{\kappa})}{k^2} (\kappa_i k_j + \kappa_j k_i) - \frac{(\mathbf{k} \cdot \boldsymbol{\kappa})^2}{k^2} \delta_{ij} - \right. \\
 & \left. - \kappa_i \kappa_j + \frac{1}{2} \left( \kappa^2 + \frac{(\mathbf{k} \cdot \boldsymbol{\kappa})^2}{k^2} \right) (\delta_{ij} - k_i k_j / k^2) \right), \quad (6.5)
 \end{aligned}$$

where  $\mathbf{k}$  and  $\boldsymbol{\kappa}$  are the wave-vectors for the small scales of turbulence and for the scale of variation of its mean characteristics (Kitchatinov & Rüdiger 2005).

The  $\Lambda$ -effect is derived in the mixing-length approximation, which will be understood as the dominance of one scale (the mixing-length) in the turbulence spectra. In this case, the spectral functions  $\hat{E}$  and  $\hat{E}_1$  can formally be written as

$$E = 2\rho^2 \langle u^{(0)2} \rangle \delta(k - \ell_{\text{corr}}^{-1}) \delta(\omega), \quad E_1 = aE/4, \quad (6.6)$$

with the proportionality coefficient  $a$ . The spectral functions can be transformed from wave space to real space, e.g.,

$$E(k, \omega, \mathbf{x}) = \int \hat{E}(k, \omega, \boldsymbol{\kappa}) \exp(i\mathbf{x} \cdot \boldsymbol{\kappa}) d\boldsymbol{\kappa}. \quad (6.7)$$

The anisotropy parameter  $a$  is not completely free. It is restricted by the condition that in the one-point-correlation tensor for the original turbulence the radial and horizontal intensities must be positive. This yields

$$-\frac{5H_\rho^2}{2\ell_{\text{corr}}^2} \leq a \leq \frac{15}{2} + \frac{5H_\rho^2}{\ell_{\text{corr}}^2}, \quad (6.8)$$

where  $H_\rho$  is the density scale height. It is assumed that the density stratification is the dominant spatial inhomogeneity.

Following the procedure described in KR93 we arrive at the expression

$$\begin{aligned} Q_{ij}^A &= \nu_T \Omega_k g_l \left( V^{(0)}(\Omega^*) (g_i \epsilon_{jkl} + g_j \epsilon_{ikl}) \right. \\ &\quad \left. - H^{(1)}(\Omega^*) \frac{(\mathbf{g} \cdot \boldsymbol{\Omega})}{\Omega^2} (\Omega_i \epsilon_{jkl} + \Omega_j \epsilon_{ikl}) \right), \end{aligned} \quad (6.9)$$

for the  $\Lambda$ -effect, with  $\mathbf{g}$  as the radial unit vector. The two parameters are

$$\begin{aligned} V^{(0)} &= \left( \frac{\ell_{\text{corr}}}{H_\rho} \right)^2 (J_0(\Omega^*) + aI_0(\Omega^*)), \\ H^{(1)} &= \left( \frac{\ell_{\text{corr}}}{H_\rho} \right)^2 (J_1(\Omega^*) + aI_1(\Omega^*)), \end{aligned} \quad (6.10)$$

where the functions  $J_0$  and  $J_1$  are the same as in KR93 but

$$\begin{aligned} I_0(\Omega^*) &= \frac{1}{4\Omega^{*4}} \left( -19 - \frac{5}{1 + \Omega^{*2}} + \frac{3\Omega^{*2} + 24}{\Omega^*} \arctan \Omega^* \right), \\ I_1(\Omega^*) &= \frac{3}{4\Omega^{*4}} \left( -15 + \frac{2\Omega^{*2}}{1 + \Omega^{*2}} + \frac{3\Omega^{*2} + 15}{\Omega^*} \arctan \Omega^* \right) \end{aligned} \quad (6.11)$$

are new. In the slow rotation case ( $\Omega^* \ll 1$ ), only the radial flux of angular momentum survives, i.e.

$$J_0 \simeq \frac{4}{15}, \quad I_0 \simeq -\frac{3}{10}, \quad J_1 \simeq I_1 \simeq O(\Omega^{*2}); \quad (6.12)$$

hence  $V^{(0)}$  is negative with  $a > 8/9$  for slow rotation.† For fast rotation ( $\Omega^* \gg 1$ ),  $J_1$  is much larger than all other functions,

$$J_1 \simeq \frac{\pi}{4\Omega^*}, \quad J_0 \simeq I_0 \simeq I_1 \simeq O(\Omega^{*-3}), \quad (6.13)$$

so that  $V < 0$  and  $H > 0$  results in this case (see Figure 6.2). Any uncertainty in the  $\Lambda$ -effect related to the unknown free  $a$ -parameter of equations (6.6) and (6.10) disappears for the most relevant application, i.e. for fast rotation.

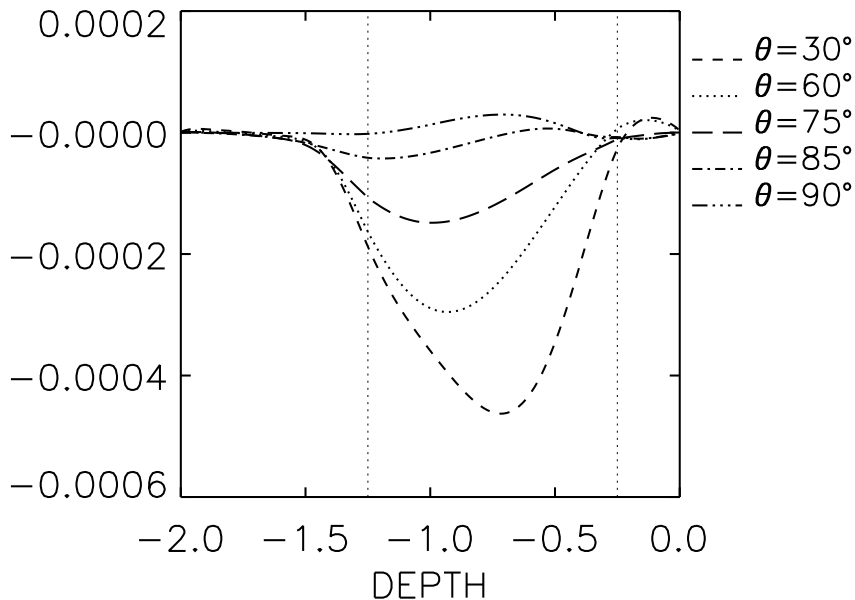


Fig. 6.3. Box simulations with NIRVANA for rotating convection. Shown is  $Q_{r\phi}$  as a function of depth, normalized with the square of the sound speed at the surface of the unstable domain.  $Ta = 10^6$ ,  $Pr = 0.1$ .

Our box simulations confirm the above findings (Figures 6.3 and 6.4). The aspect ratio of the box is 1:4, it is discretized with  $100^3$  grid points (Rüdiger, Egorov & Ziegler 2005). For  $Ta = 10^6$  the quantity  $V$  is always negative

† Opposite to the case of  $a = 0$  considered in KR93.

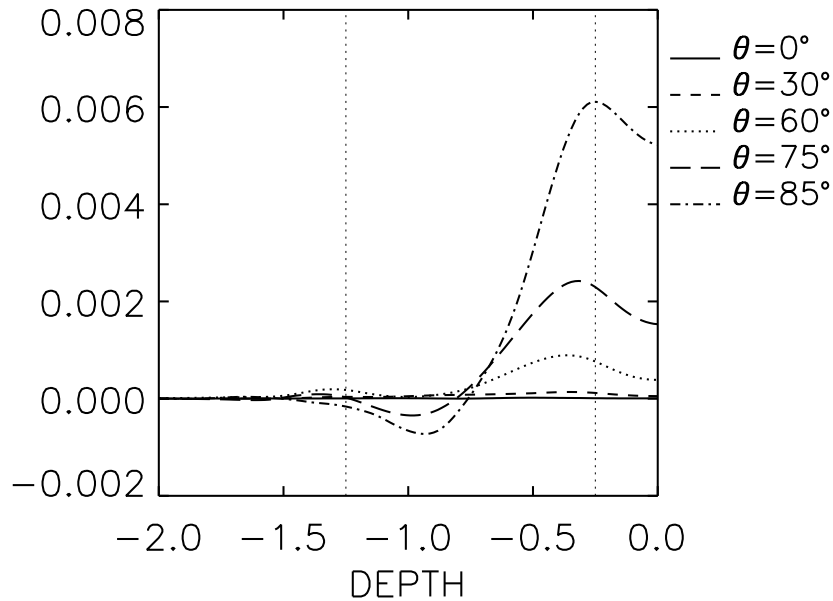


Fig. 6.4. As Fig. 6.3 but for  $Q_{\theta\phi}$ .

and becomes very small at the equator. The maximal values are reached in the middle of the box. The situation for the horizontal  $\Lambda$ -effect is more complicated. As first found by Pulkkinen *et al.* (1993), averaged over the entire box it is positive. In our simulation it dominates close to the equator and is large and positive in the top domain and small and negative in the lower half of the box.

The results of the quasilinear analytical calculations and those of the numerical simulations of the  $\Lambda$ -effect are rather close together. Though the analytical results are quasilinear *and* though they are only valid for a simplified turbulence model, the differences from the fully consistent nonlinear box simulations are rather small. The strong concentration of the horizontal angular momentum transport, however, is not yet fully understood (see also Käpylä, Korpi & Tuominen 2004; Hupfer, Käpylä & Stix 2005).

### 6.3 Turbulent heat transport

In rotating turbulent fluids the relation between the turbulent heat flux  $\mathbf{F} = \rho C_p \langle \mathbf{u}'T' \rangle$  and the superadiabatic temperature gradient  $\beta = \mathbf{g}/C_p - \nabla T$

( $\mathbf{g}$  gravity) is tensorial, i.e.

$$F_i = \rho C_p \chi_{ij} \beta_j. \quad (6.14)$$

In the simplest case without rotation it is  $\chi_{ij} = \chi_T \delta_{ij}$  so that the well-known expression  $\mathbf{F} = \rho C_p \chi_T \boldsymbol{\beta}$  results for non-rotating fluids.

There is a close relation between the heat-flux tensor and the one-point correlation tensor. We start from the quasilinear connection

$$\chi_{ij} = \iint \frac{\chi k^2 \hat{Q}_{ij}(\mathbf{k}, \omega)}{\omega^2 + \chi^2 k^4} d\mathbf{k} d\omega \quad (6.15)$$

between the spectral tensor  $\hat{Q}_{ij}$  of the turbulence and the heat-conductivity tensor  $\chi_{ij}$ . For vanishing microscopic heat conduction ( $\chi \rightarrow 0$ ) a Dirac  $\delta$ -function appears so that

$$\chi_{ij} = \pi \int \hat{Q}_{ij}(k, 0) dk \equiv \frac{1}{2} \int Q_{ij}(0, \tau) d\tau \quad (6.16)$$

results. If the  $\tau$ -integral is approximated by  $\tau_{\text{corr}}$  then  $\chi_{ij} \simeq 0.5 \tau_{\text{corr}} Q_{ij}$ . We have thus to expect that the radial heat flux follows the behavior of the radial turbulence intensity resulting from the box simulations (Figure 6.5). In the bulk of the convection box  $\langle u_r'^2 \rangle$  at the equator dominates  $\langle u_r'^2 \rangle$  at the poles. The same is indeed true for the radial heat flux derived with NIRVANA and shown in Figure 6.6 (see Rüdiger *et al.* 2005).

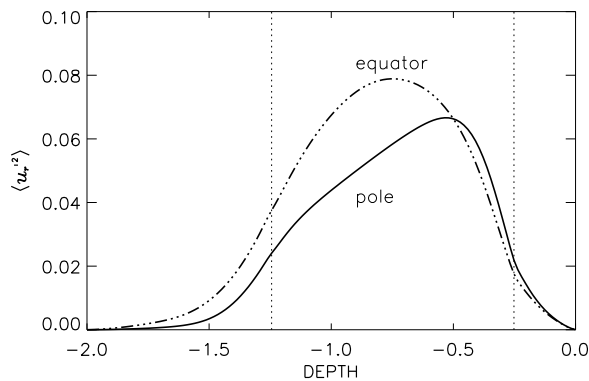


Fig. 6.5. The radial turbulence intensity (for the same convection model as used in Figs. 6.3 and 6.4). With solar values the maximal rms velocity is 300 m/s. Note that except in the top layer the turbulence at the equator exceeds the polar values. Note that a similar result also follows from box simulations without any density stratification.

Figure 6.6 (left) shows the depth-profile of the correlation  $\langle u_r' T' \rangle$  for various latitudes. Due to the rotation, the values differ between poles and the equator. The pole-equator difference in the radial heat-flux depends, however, on the radius. Except for the top layer, the eddy heat-flux at the equator exceeds the eddy heat-flux at the poles. In the top layers, where the turbulence is horizontally-dominated, the polar heat-flux dominates that at the equator. This is a characteristic but unexpected result.

Rieutord *et al.* (1994, their Figure 8a), Käpylä *et al.* (2004, their Figure 7) and Hupfer *et al.* (2005) found similar results. We are led to the conclusion that a crossover exists of the pole-equator difference in the radial eddy heat-flux almost at the same depth where the vertically-dominated turbulence changes to a horizontally-dominated turbulence. As we have demonstrated with equation (6.16) the behavior of the radial heat-flux is a direct reflection of the rotation-influenced radial turbulence intensity  $\langle u_r'^2 \rangle$ . It is shown in Figure 6.5 that in the box (except the outermost layer)  $\langle u_r'^2 \rangle$  at the equator exceeds the value at the poles.

A similar crossover does not exist for the latitudinal eddy heat-flux  $\langle u_\theta' T' \rangle$  plotted in Figure 6.6 (right). It generally vanishes at the poles and at the equator. Between these extrema the heat flows towards the pole in the convection zone and towards the equator in the lower overshoot region. This is due to the action of the Coriolis force.

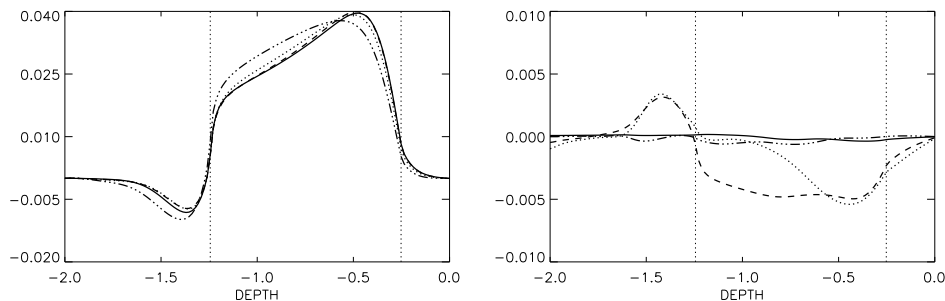


Fig. 6.6. The correlations  $\langle \mathbf{u}' T' \rangle$  vs. depth for different colatitudes in the box simulations after horizontal- and time-averaging;  $Ta = 10^6$ . Left:  $\langle u_r' T' \rangle$ . Right:  $\langle u_\theta' T' \rangle$ . Solid: pole, dashed:  $\theta = 30^\circ$ , dotted:  $\theta = 60^\circ$ , triple-dot-dashed: equator.

#### 6.4 Solar models

Differential rotation and meridional flow within the convection zone are the results of the simultaneous solution of the steady axisymmetric equations

for the momentum and the mean entropy. The models involve the  $A$ -effect defined by equations (6.9)–(6.11), which involve the only free parameter,  $a$ , while the entropy equation involves the rotation-induced anisotropic heat-flux tensor (see, however, Rempel 2005). Recent models combine the numerical simulation of the differential rotation in the convection zone with computations of the tachocline resulting from a weak internal magnetic field within the solar radiative core (details given by Kitchatinov & Rüdiger 2005). This combination of mean field hydrodynamics and magnetohydrodynamics leads to the results shown in Figures 6.7 (right) and 6.8.

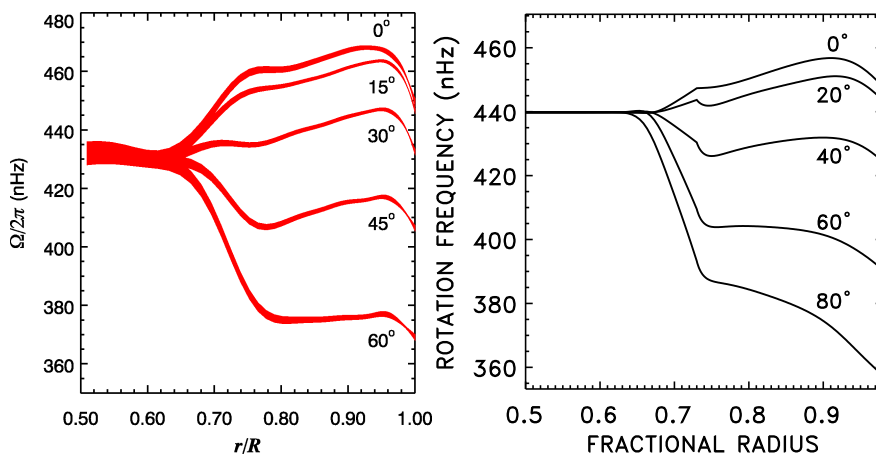


Fig. 6.7. *Left*: The internal solar rotation law as determined by helioseismology. (Courtesy NSF National Solar Observatory, see also Kosovichev *et al.* 1997.) *Right*: The rotation law from the mean-field model with a rotation period of 25 days and  $a = 2$ . The curves are marked with the latitude ( $= 90^\circ - \theta$ ).

In the simulations the anisotropy parameter is  $a = 2$  (enhanced dominance of the radial turbulence intensity), resulting in a considerably improved agreement of the rotation law in the outer supergranulation layer with helioseismological results. Our old models were computed with  $a = 0$  because there were no data for slow rotation domains to restrict its value. Now we have both better observations and the results of the numerical box simulations. The rotation laws of Figure 6.7 show a clear subsurface inward increase of the angular velocity, which may be important for the solar dynamo (Brandenburg 2005).

Even more significant may be the meridional (‘Kippenhahn’) flow as a principal ingredient of the advection-dominated dynamo models (Choudhuri, Schüssler & Dikpati 1995; Dikpati & Gilman 2001; Bonanno *et al.* 2002). The resulting meridional flow is shown in Figure 6.8. It consists of a

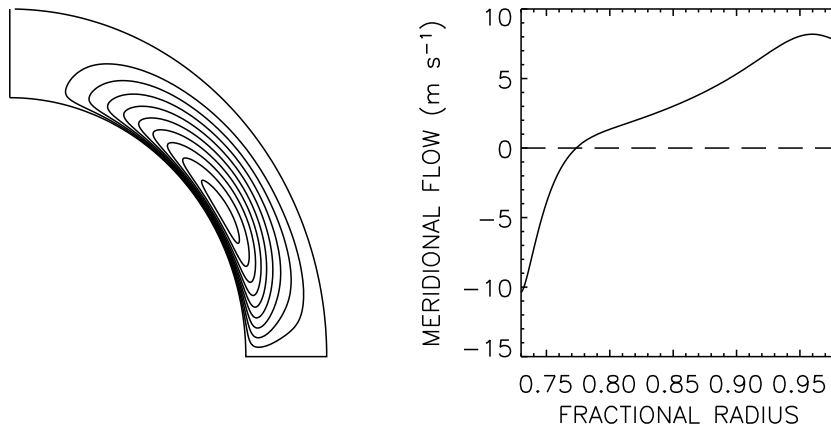


Fig. 6.8. Streamlines of the meridional flow (left) and the flow velocity for  $45^\circ$  latitude as a function of depth (right) for  $a = 2$ . Positive velocity denotes a poleward flow. One cell of anticlockwise circulation occupies the entire convection zone.

*single circulation cell* with poleward flow on the top — opposite to the result of Kippenhahn (1963). This direction of the surface flow complies with direct Doppler measurements (Komm, Howard & Harvey 1993). Helioseismology also indicates that this direction of the flow prevails to a depth of at least 12 Mm (Zhao & Kosovichev 2004). The flow reverses to the return equatorward direction somewhere deeper down. The computed return flow in Figure 6.8 has a velocity of  $\lesssim 10$  m/s at the base of the convection zone. This value suffices to transport magnetic fields towards the equator during the 11-yr cycle as required by the advection-dominated dynamo models.

Not only the flow amplitude but also the depth of its penetration into the radiative zone beneath the convection zone is important. The extent to which the penetration exists in the Sun is currently debated (Nandy & Choudhuri 2002; Gilman & Miesch 2004). Its value can be computed with the mean-field model if the bottom boundary of the simulation domain is placed inside the region of stable subadiabatic stratification. Our model applies a local mixing-length approximation. The base of the superadiabatically stratified shell, therefore, coincides with the bottom of the convection zone. A finite effective viscosity should be prescribed for the radiative core below the convection zone. The effective viscosity,  $\nu_{\text{core}}$ , can be quite small compared to the turbulent viscosity of the convection zone but must be larger than its microscopic value.

The penetration depth computed with such an approach is shown in Figure 6.9. The dependence on  $\nu_{\text{core}}$  is close to  $\sqrt{\nu_{\text{core}}}$ , in accordance with the

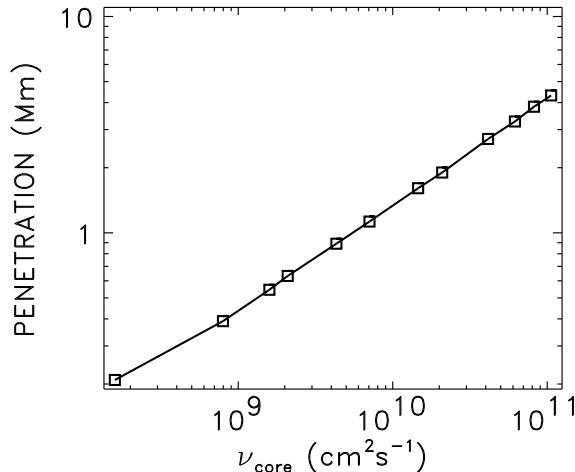


Fig. 6.9. Penetration depth  $D_{\text{pen}}$  of meridional flow into the convection zone at latitude  $45^\circ$  vs. the viscosity  $\nu_{\text{core}}$  of the convectively stable region. The dependence is very close to  $D_{\text{pen}} \propto \sqrt{\nu_{\text{core}}}$ . Squares represent the actual computations.

finding of Gilman & Miesch (2004) that the penetration under solar conditions belongs to the Ekman regime. This penetration results from viscous drag imposed by meridional flow at the base of the convection zone on the fluid beneath. The standard Ekman depth is  $D_{\text{pen}} \sim \sqrt{\nu_{\text{core}}/\Omega}$ . Such a penetration cannot play any role in a dynamo process because the time of magnetic field diffusion across the penetration layer,  $\tau_{\text{d}} \sim D_{\text{pen}}^2/\eta_{\text{core}}$ , is very small compared to the advection time,  $\tau_{\text{adv}} \sim R_{\odot}/u^{\text{m}}$ , since  $\tau_{\text{d}}/\tau_{\text{adv}} \sim Pm u^{\text{m}}/(\Omega R_{\odot}) \ll 1$ , except for the case of unrealistically large magnetic Prandtl numbers,  $Pm = \nu_{\text{core}}/\eta_{\text{core}}$  (Kitchatinov & Rüdiger 2005).

Estimation of penetration by the Ekman depth is further supported by the finding that a variation of thermal conductivity,  $\chi_{\text{core}}$ , for constant  $\nu_{\text{core}}$  does not change  $D_{\text{pen}}$ . Our computations, however, do not reproduce the Ekman relation  $D_{\text{pen}} \sim \Omega^{-0.5}$ . The slope of the dependence is not constant and is slightly larger than  $-0.5$ . The rotation rate dependence is better represented by a relation

$$D_{\text{pen}} \propto \left( \Omega^2 + \Omega \frac{\tan\theta}{2} \frac{\partial\Omega}{\partial\theta} \right)^{-0.25}. \quad (6.17)$$

Whether the viscosity  $\nu_{\text{core}}$  is large or small beneath the convection zone depends strongly on the stability of the solar tachocline. If the latter is

unstable then the viscosity is large and the penetration is deep. If, however, it is stable then the viscosity is small and the penetration is only very weak. In the hydrodynamical regime our calculations favor the small-viscosity case. If the solar tachocline is considered as a shear flow then for high enough Reynolds numbers of the rotation it is unstable for sufficiently high equator-pole differences of the angular velocity at its upper boundary.

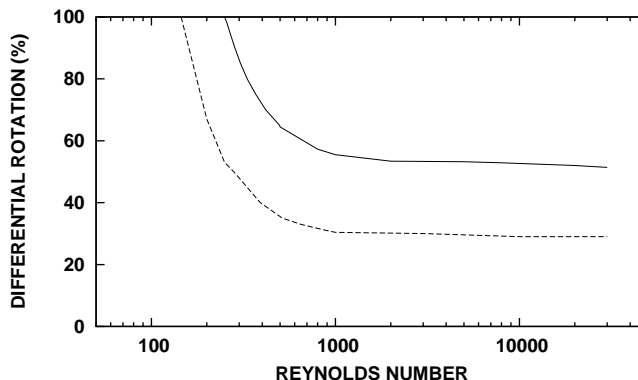


Fig. 6.10. Bifurcation map for the hydrodynamic shear instability of the solar tachocline. Dashed: only latitudinal shear, solid: rotation law  $\Omega = \Omega(r, \theta)$  taken from the helioseismology (Fig. 6.7, left). Note that the real solar tachocline is *not* unstable in the hydrodynamical regime.

The hydrodynamical stability/instability of the solar tachocline has been probed with the Hollerbach code for a shallow spherical shell subject to differential rotation (Arlt, Sule & Rüdiger 2005). If the shear is formed only by latitudinal gradients of  $\Omega$  (the Watson case) then the onset of the instability starts at about 30% of rotational shear. If, however, the radial profile of the rotation law (known from helioseismology) also enters the model then a *stronger* latitudinal shear results for the onset of the instability (Figure 6.10). We, therefore, assume the viscosity as small in the solar tachocline and the penetration of the meridional flow as weak. Of course, a final statement about this problem only depends on the solution of the stability problem in the magnetohydrodynamic regime.

## 6.5 Stellar models

Hall (1991) found differential rotation for a number of magnetically active stars from the variation of spot rotation periods over the stellar activity cycle. Messina & Guinan (2003) derived surface rotation laws from photo-

metric data of a monitoring program of stars resembling the Sun in earlier states of its evolution (Sun in time).

Unfortunately, the number of single main-sequence stars to which Doppler imaging has been successfully applied is still small (see Strassmeier 2002). For sufficiently fast rotators, surface differential rotation can be detected, however, from the broadening of spectral lines. Reiners & Schmitt (2003a,b) and Reiners (2005) carried out measurements for F stars with moderate and short rotation periods. They found differential rotation to be much more common for stars with moderate rotation rates than for very rapid rotators.

A model has been developed for the differential rotation of a main-sequence (MS) star of spectral type F8 (Küker & Rüdiger 2005). The star represents the upper end of the lower MS in the context of differential rotation and stellar activity. With a convection zone depth of 160 Mm and a surface gravity roughly equal to the solar value the main difference from the Sun is the luminosity, which is 1.7 times the solar value.

In Figure 6.11 the rotation rate is plotted vs. the radius. In all cases the equator rotates faster than the poles but the amplitude of the relative shear varies with the rotation rate. The model with the fastest rotation yields the most rigid rotation law. Note also that for fast rotation all lines are rather horizontal, i.e. there is almost no radial shear. While the isocontours are mainly radial for fast rotation the slow rotation case shows a disk-shaped pattern at high latitudes.

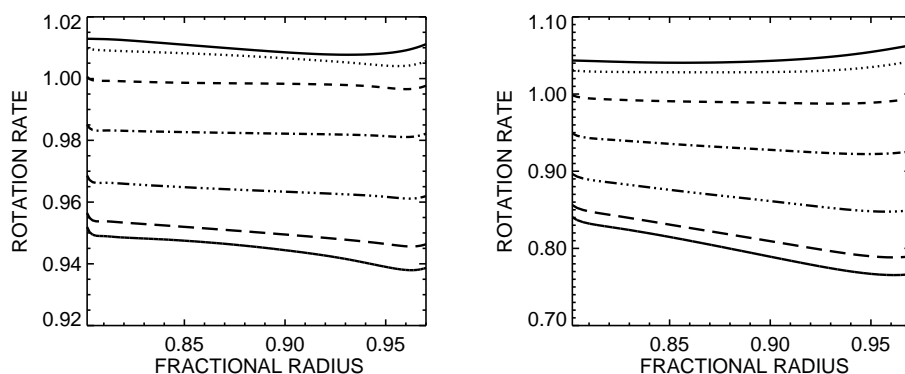


Fig. 6.11. Normalized rotation rate as a function of the stellar radius for the latitudes  $0^\circ$  (equator),  $15^\circ$ ,  $30^\circ$ ,  $45^\circ$ ,  $60^\circ$ ,  $75^\circ$ , and  $90^\circ$  (poles) (from top to bottom) for rotation periods of 4 d (left) and 14 d (right).

Figure 6.12 shows the total horizontal shear,  $\delta\Omega$ , as a function of the rotation period for various stellar models. For both F and G stars the rotation becomes more rigid for faster rotation. Between the two limiting cases the total horizontal shear has a maximum value. The period at which the maximum is reached is about one month in the case of the Sun, and 10 d for the F star. None of the curves for stars later than G shows a sharp peak. There is mostly a broad range of nearly constant shear around the maximum. The distinct maximum of the surface shear for F stars has recently been seen by Reiners (2005). Also the very clear run of the differential rotation with the effective temperature shown by the theory appears in his observational results (his Figure 5).

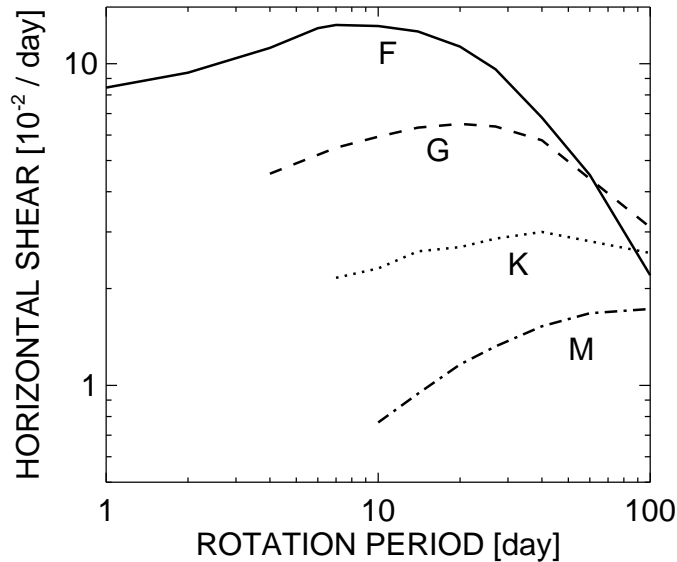


Fig. 6.12. Surface shear as a function of the rotation period and the effective temperature for MS stars marked with their spectral class

The model presented here predicts that the equatorial acceleration of lower MS stars should depend more on the luminosity rather than on the rotation rate. A possible empirical trend of the stellar differential rotation with mass and/or the rotation rate has been studied by Barnes *et al.* (2005). They found that the differential rotation decreases rapidly with decreasing mass but varies only slightly with the rotation period for a given spectral type, in general agreement with our theoretical findings.

Also AB Dor and PZ Tel, though rotating much faster than the Sun, show surface differential rotation very similar to the Sun. AB Dor and PZ Tel are PMS stars of spectral type K0 and G0 with rotation periods of 0.5 d and 1 d, respectively. With  $\delta\Omega = 0.056 \text{ d}^{-1}$  (AB Dor) and  $\delta\Omega = 0.075 \text{ d}^{-1}$  (PZ Tel) the surface shear values of these stars lie close to the solar value, with the more luminous AB Dor also showing more surface shear.

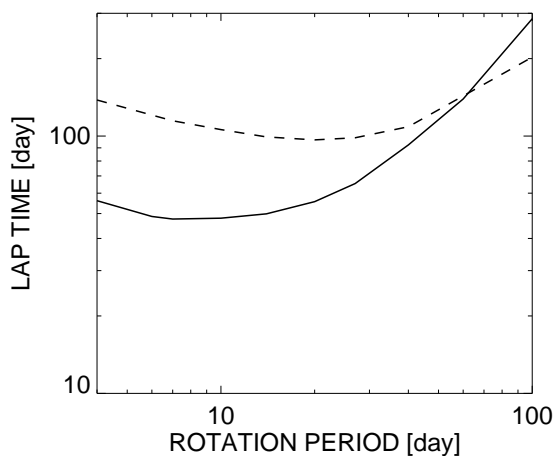


Fig. 6.13. Lap time as a function of the rotation period for the F star (solid) and the solar-type star (dashed).

Reiners & Schmitt (2003 a,b) found values between 10 and 30 days for the lap time  $2\pi/\delta\Omega$ . Figure 6.13 shows the lap time vs. the rotation period for the F and G stars. For both types of stars there is little variation except for very long periods where the lap time strongly increases. The value for the solar-type star is about 100 d at the period of maximum shear. In Figure 6.14 the maximum flow speed at the bottom of the convection zone of the F star is shown. A positive sign means that the flow is toward the equator, negative values indicate poleward flow. For the F8 star the value of the drift decreases from 10 m/s for  $P_{\text{rot}} = 4 \text{ d}$  to very small values for  $P = 30 \text{ d}$ . A possible change of the flow direction at the bottom of the convection zone should have dramatic consequences for the stellar dynamo if indeed the form of the butterfly diagram is dominated by the meridional flow at the bottom of the convection zone.

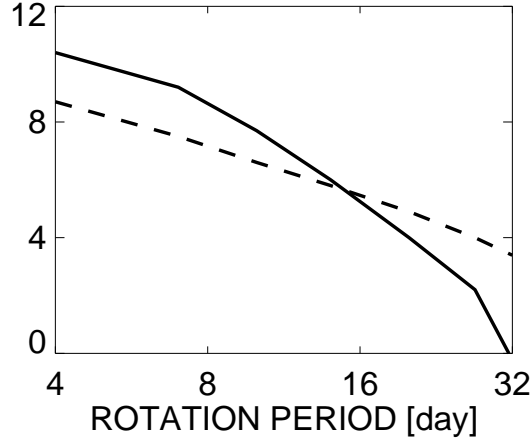


Fig. 6.14. Meridional flow speed in m/s at the bottom of the convection zone as a function of the rotation period. Positive values correspond to gas motion toward the equator. Solid: F8 star. Dashed: G star. (From Küker & Rüdiger 2005.)

### 6.6 Antisolar rotation?

Hydrodynamical models of stellar rotation always lead to solar-type rotation with an accelerated equator. Observations confirm that it is indeed the typical case (Petit, Donati & Collier Cameron 2004). However, observational indications of antisolar rotation are numerous enough to demand a consideration of its possible origin.

The clearest possibility for a faster rotation of high latitudes is a rapid meridional flow  $u^m$ . The flow provides a uniform angular momentum along the streamlines when the Reynolds number

$$\text{Re} = \frac{u^m R_\odot}{\nu_T} \quad (6.18)$$

is sufficiently large, thus ensuring antisolar rotation (Rüdiger 1989). A polar vortex results for both directions of the meridional flow. The required Reynolds number depends on the sense of the flow. A faster polar rotation is easier to produce by a flow which is poleward on the top. A moderate  $\text{Re} \lesssim 100$  can be sufficient in this case.

However, the meridional flow computed with the mean-field models is not fast enough. The Reynolds number for the solar model of §6.4 is  $\lesssim 10$ . An additional driver of meridional circulation is thus required for antisolar rotation. Barocline forcing from magnetic-induced large-scale thermal in-

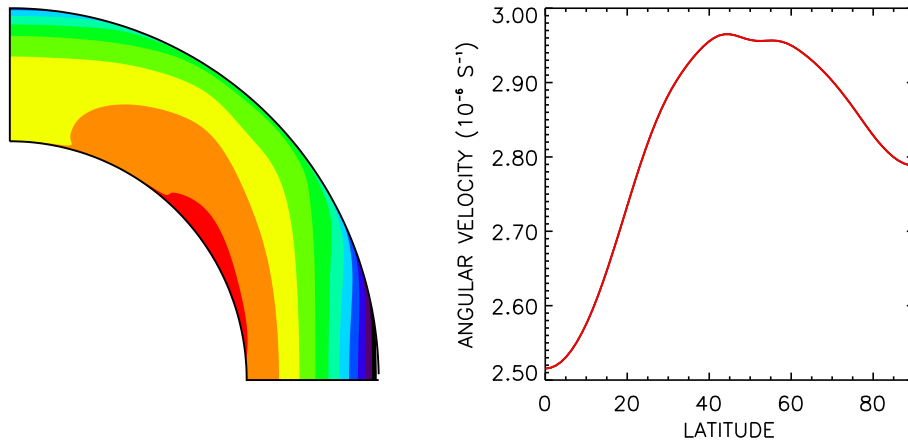


Fig. 6.15. A characteristic rotation law resulting under the presence of a poloidal magnetic field with an amplitude of 200 Gauss on a giant star. The angular velocity increases from the equator to the poles by  $\sim 10\%$ .

homogeneities (or tidal forcing by a close companion) is the possible driver (Kitchatinov & Rüdiger 2004). Figure 6.15 shows the resulting rotation law for a magnetic field involved through the boundary condition of a steady radial field penetrating the convection zone at the inner boundary from the radiative core. The bottom field is prescribed by a steady potential at the inner boundary, which can be understood as the penetration of a relic field stored in the radiative core into the convection zone.

This concept is favored by the observations (Strassmeier 2004). Among nine examples of antisolar rotation he reports six belonging to close binaries and two to giant stars with large dark spots on their surfaces. The remaining star is LQ Hya for which different observations disagree about the sense of its differential rotation (perhaps, because it strongly varies with time, see Donati, Cameron & Petit 2003). Recently Weber, Strassmeier & Washuettl (2005) suggest that antisolar rotation on giant stars may indeed be accompanied by a fast ( $\sim 1000$  m/s) poleward surface flow.

**Acknowledgements.** L.L.K. is grateful to the Alexander v. Humboldt Foundation for support. Thanks are due also to the Russian Foundation for Basic Research (Project 05-02-16326).

## References

Arlt, R., Sule, A. & Rüdiger, G. (2005). *Astron. Astrophys.* **441**, 1171.

- Barnes, J.R., Cameron, A.C., Donati, J.-F., James, D.J., Marsden, S.C. & Petit, P. (2005). *Mon. Not. Roy. Astron. Soc.* **357**, L1.
- Bonanno, A., Elstner, D., Rüdiger, G. & Belvedere, G. (2002). *Astron. Astrophys.* **390**, 673.
- Brandenburg, A. (2005). *Astrophys. J.* **625**, 539.
- Choudhuri, A.R., Schüssler, M. & Dikpati, M. (1995). *Astron. Astrophys.* **303**, L29.
- Dikpati, M. & Gilman, P.A. (2001). *Astrophys. J.* **559**, 428.
- Donati, J.-F., Cameron, A.C. & Petit, P. (2003). *Mon. Not. Roy. Astron. Soc.* **345**, 1187.
- Gilman, P.A. & Miesch, M.S. (2004). *Astrophys. J.* **611**, 568.
- Hall, D.S. (1991). In *The Sun and Cool Stars: Activity, Magnetism, Dynamos*, ed. I. Tuominen, D. Moss & G. Rüdiger (Springer-Verlag, Berlin), p. 353.
- Hupfer, C., Käpylä, P.J. & Stix, M. (2005). *Astron. Nachr.* **326**, 223.
- Käpylä, P.J., Korpi, M.J. & Tuominen, I. (2004). *Astron. Astrophys.* **422**, 793.
- Kippenhahn, R. (1963). *Astrophys. J.* **137**, 664.
- Kitchatinov, L.L. & Rüdiger, G. (1993). *Astron. Astrophys.* **276**, 96 (KR93).
- Kitchatinov, L.L. & Rüdiger, G. (2004). *Astron. Nachr.* **325**, 496.
- Kitchatinov, L.L. & Rüdiger, G. (2005). *Astron. Nachr.* **326**, 379.
- Komm, R.W., Howard, R.F. & Harvey, J.W. (1993). *Sol. Phys.* **147**, 207.
- Kosovichev, A.G. & 33 others (1997). *Sol. Phys.* **170**, 43.
- Küker, M. & Rüdiger, G. (2005). *Astron. Astrophys.* **433**, 1023.
- Messina, S. & Guinan, E.F. (2003). *Astron. Astrophys.* **409**, 1017.
- Nandy, D. & Choudhuri, A.R. (2002). *Science* **296**, 1671.
- Petit, P., Donati, J.-F. & Cameron, A.C. (2004). *Astron. Nachr.* **325**, 221.
- Pulkkinen, P.J., Tuominen, I., Brandenburg, A., Nordlund, A. & Stein, R.F. (1993). *Astron. Astrophys.* **267**, 265.
- Reiners, A. & Schmitt, J.H.M.M. (2003a). *Astron. Astrophys.* **398**, 647.
- Reiners, A. & Schmitt, J.H.M.M. (2003b). *Astron. Astrophys.* **412**, 813.
- Reiners, A. (2005). *Astron. Astrophys.* (in press).
- Rempel, M. (2005). *Astrophys. J.* **622**, 1320.
- Rieutord, M., Brandenburg, A., Mangeney, A. & Drossart, P. (1994). *Astron. Astrophys.* **286**, 471.
- Rüdiger, G. (1989). *Differential Rotation and Stellar Convection: Sun and Solar-Type Stars* (Gordon and Breach Science Publishers, New York).
- Rüdiger, G., Egorov, P., Kitchatinov, L.L. & Küker, M. (2005). *Astron. Astrophys.* **431**, 345.
- Rüdiger, G., Egorov, P. & Ziegler, U. (2005). *Astron. Nachr.* **326**, 315.
- Strassmeier, K.G. (2002). *Astron. Nachr.* **323**, 309.
- Strassmeier, K.G. (2004). In *Stars as Suns*, ed: A.K. Dupree & A.O. Benz (ASP), p. 11.
- Weber, M., Strassmeier, K.G. & Washuettl, A. (2005). *Astron. Nachr.* **326**, 287.
- Zhao, J. & Kosovichev, A.G. (2004). *Astrophys. J.* **603**, 776.